Chemical Science

ROYAL SOCIETY OF CHEMISTRY

EDGE ARTICLE

View Article Online
View Journal | View Issue

Check for updates

Cite this: *Chem. Sci.*, 2021, **12**, 15533

All publication charges for this article have been paid for by the Royal Society of Chemistry

Received 15th September 2021
Accepted 15th November 2021

DOI: 10.1039/d1sc05112a

rsc.li/chemical-science

Open Access Article. Published on 15 November 2021. Downloaded on 2/20/2026 10:56:39 PM. This article is licensed under a Creative Commons Attribution-NonCommercial 3.0 Unported Licence.

Multi-stimuli programmable FRET† based RGB absorbing antennae towards ratiometric temperature, pH and multiple metal ion sensing‡

Kavita Rani and Sanchita Sengupta *

A red-green-blue (RGB) multichromophoric antenna **1** consisting of energy donors naphthalimides and perylenediimides and a central aza-BODIPY energy acceptor along with two subchromophoric red-blue (RB **6**) and green-blue (GB **12**) antennae was designed that showed efficient cascade Förster resonance energy transfer (FRET). RGB antenna **1** showed pronounced temperature-dependent emission behaviour where emission intensities in green and red channels could be tuned in opposite directions by temperature giving rise to unique ratiometric sensing with a temperature sensitivity of 0.4% °C. RGB antenna **1** showed reversible absorption modulation selectively in the blue region (RGB ↔ RG) upon acid/base addition giving rise to pH sensing behaviour. Furthermore, RGB antenna **1** was utilized to selectively sense metal ions such as Co^{2+} and Fe^{3+} through a FRET turn-off mechanism induced by a redox process at the aza-BODIPY site that resulted in the selective spectral modulation of the red band (*i.e.*, RGB → GB). Model antenna RB **6** showed white light emission with chromaticity coordinates (0.32, 0.33) on acid addition. Antennae **1**, **6** and **12** also exhibited solution state electrochromic switching characterized by distinct colour changes upon changing the potential. Finally, antennae **1**, **6** and **12** served as reversible fluorescent inks in PMMA/antenna blends whereby the emission colours could be switched or tuned using different stimuli such as acid vapour, temperature and metal ions.

Introduction

Photosynthesis is initiated by capturing of sunlight by light harvesting (LH) antennae followed by rapid excitation energy transfer and has been an area of intense activity since decades.[1–5] Natural photosynthetic systems contain LH antennae that absorb in the complementary regions of the solar spectrum ultimately leading to panchromatic absorption.[6,7] Efficient harvesting of sunlight can be achieved by using biomimetic architectures,[8] with intense and panchromatic absorption in the red-green-blue (RGB) region. Such architectures can be constructed by carefully choosing chromophores absorbing in these three regions of the solar spectrum that show ultrafast intrachromophoric energy transfer and are photochemically robust.[8] Multiple reports of artificial LH arrays constructed either through covalent bonds[2,9] such as dendrimers,[10–13] conjugated polymers,[14] multichromophoric arrays[8,9,15,16] or non-covalent achitectures[8,17–20] are available. However, the majority of the reported covalent multichromophoric LH systems are based on the one step Förster resonance energy transfer (FRET) process between the energy donor and energy acceptor.[21] Covalently connected LH systems based on two step energy transfer, panchromatic absorption and large Stokes shift are suitable for multiple sensing and imaging applications.[22] Reports on two step cascade energy transfer based multichromophoric RGB LH systems are achieved mostly through dendritic design[23–27] such as dendritic solar concentrators,[28] arrays,[13,29–31] small molecule based funnels,[9,32,33] heterotriads[34] and templated chromophore assemblies on peptide scaffolds,[35] DNA scaffolds[36] and organic nanostructures.[37] FRET based LH systems have also been utilized in organic photovoltaics,[38] photocatalysis,[39] photodynamic therapy,[40] bioimaging,[41] ratiometric temperature sensing and ion sensing[21,42–44] in recent years.

Materials which show modulation of physiochemical properties with external stimuli such as pH, heat, chemicals, electricity have been under extensive research in the last few years.[45–47] Owing to multiple absorption and emission bands of RGB systems, it is possible to modulate their spectral properties by selectively tuning the bands by some kind of external stimuli such as temperature, pH and so on. RGB systems incorporated into polymers have been successfully utilized for modulating and switching their two- and three-state absorption or emission using external stimuli such as pH, temperature and so on.[45,46,48–52] However, to the best of our knowledge, covalently connected small molecule based RGB antennae that exhibit

Department of Chemical Sciences, Indian Institute of Science Education and Research (IISER), Mohali, Punjab-140306, India. E-mail: sanchita@iisermohali.ac.in

† Förster resonance energy transfer.

‡ Electronic supplementary information (ESI) available. See DOI: 10.1039/d1sc05112a

© 2021 The Author(s). Published by the Royal Society of Chemistry

Open Access Article. Published on 15 November 2021. Downloaded on 2/20/2026 10:56:39 PM. This article is licensed under a Creative Commons Attribution-NonCommercial 3.0 Unported Licence.

FRET and serve as multiparameter sensors through the selective modulation of the different absorption or emission bands by external stimuli, have not been reported. Covalently connected multichromophoric RGB antenna systems are synthetically much more challenging to achieve compared to supramolecular or polymeric designs. However, the former provides several advantages such as high purity, monodispersity, synthetic scalability, solubility and facile tunability of structural and optical properties over supramolecular or polymeric systems. Herein, we report a RGB LH antenna **1** (Fig. 1) consisting of eleven chromophores that are covalently connected with eight 1,8-naphthalimides (Np)[53] (blue absorber) as primary donors, two perylenediimides (PDI)[54] (green) as primary acceptors and one aza-BODIPY[55] (red) as the secondary acceptor for cascade FRET. 1,8-Np was selected as the blue (B) light absorbing chromophore due to its high fluorescence quantum yield and excellent photothermal and chemical stability.[53] PDI being one of the most versatile and well-studied chromophores owing to its near-unity fluorescence quantum yield, outstanding (photo) chemical and thermal stability and intense absorption in the visible region was utilized as the green (G) chromophore.[54] Aza-BODIPY with intense absorption in the near-infrared (NIR) region, high fluorescence quantum yield, good photo and thermal stability and wide applications as optical sensors and optoelectronic materials[55] was employed as the red (R) chromophore. Np connected to the PDIs through bay positions *via* the non-conjugated phenoxy linker and further PDI-$(Np)_4$ connected to aza-BODIPY through triazole rings *via* the click reaction ensure the preclusion of any electronic communication between donor and acceptor chromophores. The RGB antenna **1** showed ~100% FRET to either PDI or to aza-BODIPY upon photoexcitation of Np. Subchromophoric RB antenna **6** and GB antenna **12** were also synthesized and studied in detail (Fig. 1). In addition to efficient cascade FRET, the designed antennae RGB **1**, RB **6** and GB **12** showed selective modulation of their various absorption and emission bands by application of external stimuli such as pH, metal ions, and temperature and redox stimuli. Such prominent multi stimuli responsive absorption and emission modulation leading to pH sensing, ratiometric temperature sensing, multiple metal ion sensing by FRET turn-off and electrochromic switching can lead to pronounced multiparameter sensing in cellular microenvironments using these molecular antennae.

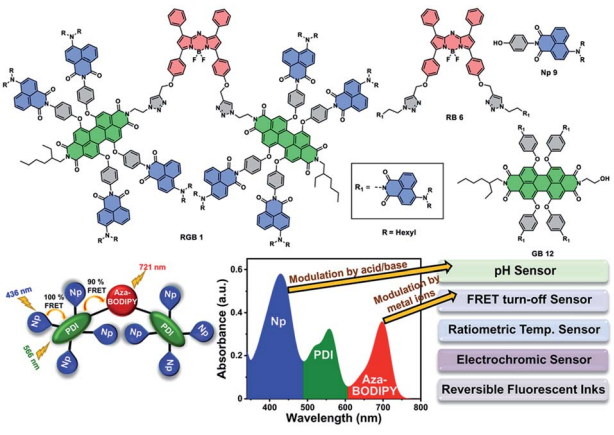

Fig. 1 Chemical structures of RGB antenna **1**, RB **6** and GB **12**, and Np **9** and schematic representation of the RGB antenna for multiparameter sensing.

Results and discussion

Synthesis

The detailed synthetic routes and experimental procedures for RGB antenna **1** and the model antennae RB **6** and GB **12** are described in Scheme S1–S4 in the ESI.‡ The model antenna RB **6** was synthesized by the copper(I) catalysed azide–alkyne cycloaddition (CuAAC) reaction between Np **4** and aza-BODIPY **5** in 78% yield (Scheme 1) and model antenna GB **12** was synthesized by nucleophilic substitution of PDI compound **11** at its bay positions with Np **9** in 33% yield (Scheme S3‡). Subsequently, GB **12** was converted from the alcoholic to azide functionality for further reaction with aza-BODIPY **5** by the CuAAC reaction to obtain the final RGB antenna **1** in 82% yield as a brown colour solid (Scheme 2). All the intermediates and final compounds were characterized structurally using ^{1}H NMR, ^{13}C NMR and HRMS/MALDI techniques.

Photophysical properties

The photophysical properties of RGB antenna **1**, RB **6** and GB **12** were investigated using UV/Vis absorption, steady state fluorescence, fluorescence quantum yield and fluorescence lifetime measurements. The absorption and emission properties of RGB antenna **1**, RB **6** and GB **12** were investigated in chloroform ($CHCl_3$) (Fig. 2a and b) and summarized in Table 1. RB **6** exhibited two absorption bands at 442 nm and 688 nm

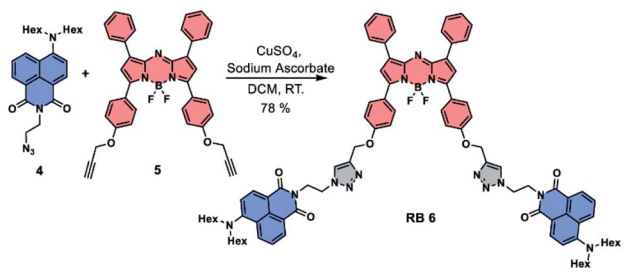

Scheme 1 Synthesis of RB antenna **6**.

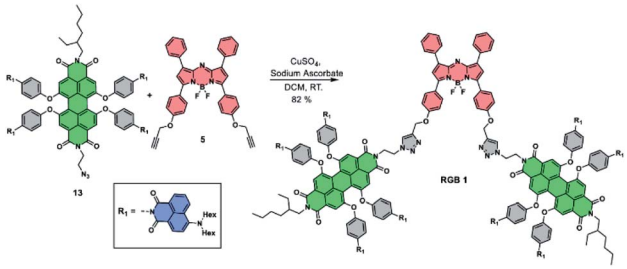

Scheme 2 Synthesis of RGB antenna **1**.

© 2021 The Author(s). Published by the Royal Society of Chemistry

Open Access Article. Published on 15 November 2021. Downloaded on 2/20/2026 10:56:39 PM.
This article is licensed under a Creative Commons Attribution-NonCommercial 3.0 Unported Licence.

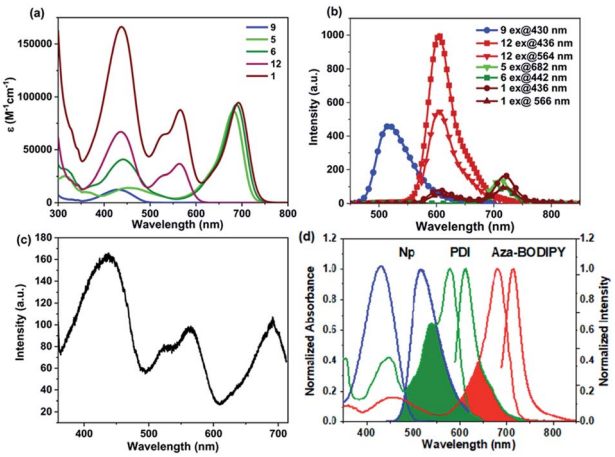

Fig. 2 (a) UV/Vis spectra, (b) emission spectra of Np **9**, aza-BODIPY **5**, RB **6**, GB **12** and RGB **1** in $CHCl_3$ ($c \sim 2 \times 10^{-6}$ M); (c) fluorescence excitation spectrum of RGB antenna **1** at $\lambda_{em} = 721$ nm of aza-BODIPY; (d) spectral overlap of emission spectra of energy donors and absorption spectra of energy acceptors for the constituent chromophores of RGB antenna **1**.

corresponding to Np and aza-BODIPY respectively and GB **12** showed two absorption bands at 436 nm and 564 nm corresponding to Np and PDI respectively. RGB antenna **1** exhibited panchromatic absorption with three well-separated absorption bands at 436 nm, 566 nm and 693 nm corresponding to Np, PDI and aza-BODIPY respectively which further facilitate their selective photoexcitation and it has a brown colour indicating the spectral sum of blue, green and red colours. Constituent chromophores retaining their spectral identity in the final RGB antenna indicate that there is no ground state electronic interaction between them.

The primary energy donor Np **9** showed high emission intensity upon excitation at 430 nm; however, for model antennae RB **6**, GB **12** and RGB antenna **1**, the emission intensity of Np was quenched by ~99% and simultaneously we observed emission from PDI and aza-BODIPY moieties which is indicative of FRET from Np to PDI or to aza-BODIPY (Fig. 2b). Further in RGB antenna **1** on direct excitation of primary energy acceptor PDI the emission intensity was quenched by ~90% compared to model antenna GB **12** indicative of FRET from PDI to aza-BODIPY (Fig. 2b). Fluorescence excitation spectra were recorded for RB **6**, GB **12** (Fig. S1‡) and RGB antenna **1** (Fig. 2c) in chloroform by holding emission monochromator at the λ_{em} of corresponding energy acceptors. For RGB antenna **1**, the excitation spectra (Fig. 2c) consisted of the bands of all the constituent chromophores Np, PDI and aza-BODIPY, recorded at an emission wavelength of 721 nm (aza-BODIPY emission), clearly revealing efficient FRET from Np and PDI to aza-BODIPY. Fig. 2d represents the efficient spectral overlap of emission spectra of the primary donor (Np) and absorption spectra of the primary energy acceptor (PDI), and emission spectra of the secondary donor (PDI) and absorption spectra of the secondary acceptor (aza-BODIPY) which is an essential pre-requisite for efficient FRET.

Further, from the reduction of fluorescence quantum yields (Table S1‡) of the reference energy donors, the energy transfer efficiencies (ETEs) (Table S2‡) were calculated to be ~100% for model antennae RB **6**, GB **12** and RGB antenna **1**.

To further confirm the energy transfer process in RB **6**, GB **12** and RGB **1**, time resolved fluorescence measurements were performed by the time correlated single photon counting (TCSPC) technique in $CHCl_3$ and fluorescence lifetimes are summarised in Table S3.‡ The reference energy donor Np **9** on excitation at 440 nm exhibited a lifetime of 7.93 ns while in RB **6**, GB **12** and RGB **1** on excitation at 440 nm (Np excitation), lifetime was reduced to 0.027 ns (99%), 0.006 ns (100%) and 0.008 ns (100%) which could be attributed to energy transfer from donor(s) to the acceptor in all the antennae. Furthermore, RGB **1** on excitation at 560 nm (PDI excitation) exhibited one shorter decay component of 3.59 ns (contribution of 29%) which is due to energy transfer from PDI to aza-BODIPY and a longer decay component of 5.88 ns (65%) due to PDI emission. For RB **6**, while monitoring the acceptor emission, lifetime was higher upon donor (Np) excitation (3.08 ns, 100%) compared to direct acceptor (aza-BODIPY) excitation (2.83 ns, 100%) which is indicative of FRET from Np to aza-BODIPY. Even though the spectral overlap of Np emission and aza-BODIPY absorption is minimal, FRET occurs in the present system as is reported for several orthogonally arranged chromophores or chromophores with minimal spectral overlap.[56–59] For GB **12**, fluorescence lifetime on direct acceptor excitation (5.95 ns, 100%) was almost comparable to donor (Np) excitation (5.69 ns with 86% contribution). For RGB **1**, while monitoring the acceptor emission channel, fluorescence lifetimes for direct acceptor (aza-BODIPY) excitation (2.51 ns), donor (Np) excitation (2.27 ns) and donor (PDI) excitation (2.57 ns) were comparable. The ETEs calculated from fluorescence lifetimes for all three antennae are shown in Table S4.‡

Solvent polarity dependent absorption and emission spectra were recorded for antennae RB **6**, GB **12** and RGB antenna **1** (Table S5‡) and ETEs were calculated to be ~90–100% (Table S6‡) by comparing the emission intensities with reference

Table 1 Photophysical parameters of Np **9**, aza-BODIPY **5**, RB **6**, GB **12** and RGB **1** in $CHCl_3$

Comp.	λ_{abs} (nm)	ε(M^{-1} cm^{-1})	λ_{em} (nm)
9	430	12 360	518
5	682	86 747	714
6	442, 688	40 683 (442), 92 619 (688)	518, 717 (λ_{ex} = 442 nm), 717 (λ_{ex} = 688 nm)
12	436, 564	66 886 (436), 36 614 (564)	518, 606 (λ_{ex} = 436 nm), 606 (λ_{ex} = 564 nm)
1	436, 566, 693	166 285 (436), 87 694 (566), 95 549 (693)	606, 721 (λ_{ex} = 436 nm), 606, 721 (λ_{ex} = 566 nm), 723 (λ_{ex} = 693 nm)

© 2021 The Author(s). Published by the Royal Society of Chemistry

Open Access Article. Published on 15 November 2021. Downloaded on 2/20/2026 10:56:39 PM. This article is licensed under a Creative Commons Attribution-NonCommercial 3.0 Unported Licence.

energy donors (Fig. S2–S4‡) which is indicative of the fact that FRET is the major deactivation pathway in all these antennae (explained in detail in the ESI‡).

Ratiometric temperature sensing

Owing to their multiple channel emissions, ratiometric temperature sensing behaviour was elucidated by monitoring the emission in all the channels of these compounds at different temperatures. Such ratiometric sensing has several advantages such as internal self-calibration and inertness to instrumental parameters or light intensity and sample concentration and thus are highly advantageous over single emission intensity-based temperature sensors.[43] Temperature-dependent fluorescence spectra were recorded for RB **6**, GB **12** and RGB antenna **1** in $CHCl_3$ in the temperature range −10 °C to +60 °C.

For RB **6**, an increase in temperature led to a blue shift and a decrease in the emission intensity of the aza-BODIPY band at 717 nm which could be attributed to thermal quenching while emission of Np at 518 nm remained unchanged (Fig. 3a). From the plot of $I_{518}/I_{518} + I_{717}$ *vs.* temperature, temperature sensitivity was calculated to be 0.1% °C (Fig. 3b). For GB **12**, an increase in temperature led to an increase in the intensity of the PDI band at 606 nm which could be due to an increase in FRET efficiency from Np to PDI with a rise in temperature from Np to PDI (Fig. 3c) and varying the temperature sensitivity from 0.015% °C to 0.001% °C (Fig. 3d and S5‡). For RGB antenna **1**, increase in temperature led to an increase in the emission intensity of the PDI band (606 nm) and a concomitant decrease in the intensity of the aza-BODIPY band (721 nm) which indicates FRET modulation *i.e.*, decreased FRET between PDI and aza-BODIPY upon increasing the temperature (Fig. 3e). The FRET modulation could be attributed to temperature induced conformational changes that might change the transition dipole orientations and thus the extent of FRET.[44,60] Temperature dependent UV/Vis spectra were mostly unchanged for all compounds (Fig. S6‡).

Even though the two bands changed in opposite directions upon increasing the temperature for **1**, their ratio $I_{606}/I_{606} + I_{721}$ showed a linear dependence with temperature and a temperature sensitivity of 0.4% °C (Fig. 3f). Such ratiometric temperature sensing behaviour with two bands changing in opposite directions has been rarely reported for organic chromophoric systems.[61]

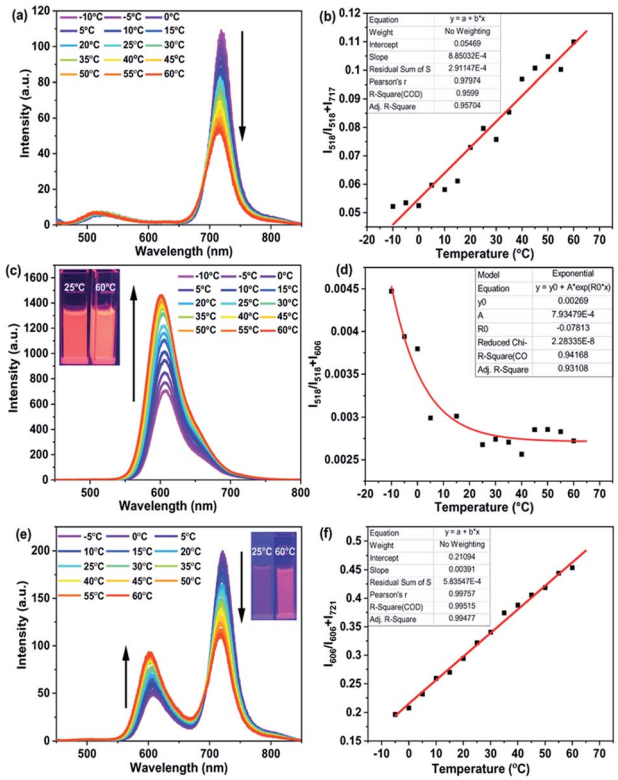

Fig. 3 Temperature-dependent emission spectra of (a) RB **6**, (c) GB **12** and (e) RGB **1** in $CHCl_3$ ($c \sim 2 \times 10^{-6}$ M); plot of (b) $I_{518}/I_{518\,+\,717}$ *vs.* temperature (RB **6**), (d) $I_{518}/I_{518\,+\,606}$ *vs.* temperature (GB **12**) and (f) $I_{606}/I_{606\,+\,721}$ *vs.* temperature (RGB **1**). Insets of (c) and (e) show the solution colours at two different temperatures under 365 nm UV lamp illumination.

Electrochemical properties and electrochromism

Redox properties of RGB antenna **1**, RB **6** and GB **12** were assessed by cyclic voltammetry measurements (Fig. S7‡) and the frontier molecular orbital energy levels (HOMO and LUMO) were calculated for all molecules (Fig. S8‡ and Table 2). The HOMO levels of RGB antenna **1**, RB **6** and GB **12** were obtained as −5.75 eV, −5.76 eV and −5.73 eV. The deep lying HOMO levels of the antenna **1**, RB **6** and GB **12** indicate their resistance to aerial oxidation and high ambient stability. Furthermore, LUMO levels of −4.33 eV, −4.53 eV and −4.48 eV were obtained for RGB antenna **1**, RB **6** and GB **12** respectively indicative of strong electron deficient behaviour of these compounds, desired pre-requisites for (opto)electronic applications.

In order to elucidate the effect of redox stimuli on spectral properties, spectroelectrochemistry was performed for reference chromophore Np **9** (Fig. S9‡), model antennae RB **6** and GB **12** and final RGB antenna **1**. RB antenna **6** during oxidation showed depletion of the absorption band at 440 nm characteristic of $Np^{+\bullet}$ formation (Fig. 4a), depletion of the 688 nm band and new band emergence at ∼760 nm corresponding to aza-$BODIPY^{+\bullet}$ formation. In the reduction cycle, the depletion

Table 2 Redox properties of compounds **9**, RB **6**, GB **12** and RGB **1**

Property	**9**	**6**	**12**	**1**
E_{ox}^{onset} (V)	+1.14	+1.00	+0.97	+0.99
E_{red}^{onset} (V)	−1.35	−0.23	−0.28	−0.43
λ_{onset} (nm)	490	735	611	742
HOMO[a] (eV)	−5.90	−5.76	−5.73	−5.75
LUMO[b] (eV)	−3.41	−4.53	−4.48	−4.33
E_g^{optc}	2.53	1.69	2.03	1.67
E_g^{cv} (eV)	2.49	1.23	1.25	1.42

[a] HOMO = $-(E_{ox}^{onset} + 4.76)$ eV, where E_{ox}^{onset} is first oxidation onset. [b] LUMO = $-(E_{red}^{onset} + 4.76)$ eV, where E_{red}^{onset} is first reduction onset. [c] $E_g^{opt} = 1241/\lambda_{onset}$.

© 2021 The Author(s). Published by the Royal Society of Chemistry

Open Access Article. Published on 15 November 2021. Downloaded on 2/20/2026 10:56:39 PM. This article is licensed under a Creative Commons Attribution-NonCommercial 3.0 Unported Licence.

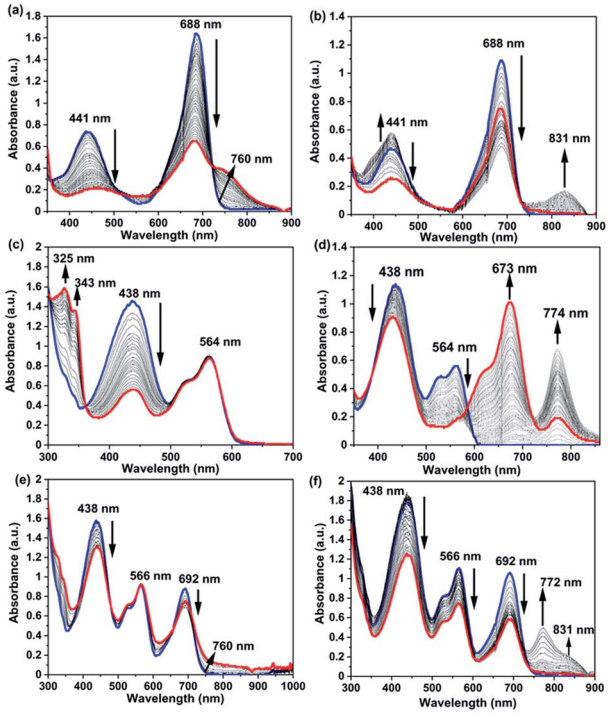

Fig. 4 Spectroelectrochemical changes observed for (a), (b) RB **6**, (c), (d) GB **12** and (e), (f) RGB antenna **1** in DCM during the oxidation (0 to +2 V) and reduction process (0 to −2 V) respectively. Initial and final spectra are represented by blue and red colours respectively.

of the absorption band at 441 nm indicated the formation of $Np^{-\bullet}$ and 688 nm band depletion and new band formation at 831 nm indicated the formation aza-BODIPY$^{-\bullet}$ (Fig. 4b). GB antenna **12** showed the Np band depletion at 438 nm corresponding to the formation of $Np^{+\bullet}$ and $Np^{-\bullet}$ while the PDI band at 564 nm remained unaffected during the oxidation cycle (Fig. 4c). In the reduction cycle, the Np band at 438 nm depleted and the PDI band at 564 nm depleted with concomitant emergence and disappearance of two new bands at 673 nm and 774 nm indicating the formation of $PDI^{-\bullet}$ and $PDI^{2-\bullet}$ (Fig. 4d).

RGB antenna **1** showed the same effect as that of subchromophoric parts, showing depletion of the Np band at 438 nm during both oxidation and reduction corresponding to the formation of $Np^{+\bullet}$ and $Np^{-\bullet}$ respectively and the PDI band at 566 nm remained unaffected during the oxidation cycle. In the reduction cycle, the PDI band was depleted and new bands emerged and disappeared at ~688 nm and at 772 nm corresponding to the formation of $PDI^{-\bullet}$ and $PDI^{2-\bullet}$. Aza-BODIPY$^{+\bullet}$ was characterized by depletion at 692 nm and formation of a shoulder at 760 nm during the oxidation cycle while the reduction cycle showed the depletion of the band at 692 nm and emergence of a new band at 831 nm for aza-BODIPY$^{-\bullet}$ formation (Fig. 4e and f). The corresponding changes in colour while applying the redox stimuli on RB **6**, GB **12** and RGB **1** are depicted in Fig. 5. RB **6** which was initially light green in the neutral state turned to olive green either on oxidation or on reduction and reverted back to the initial colour in back cycles (Fig. 5). GB **12** was dark orange in the neutral state and it turned

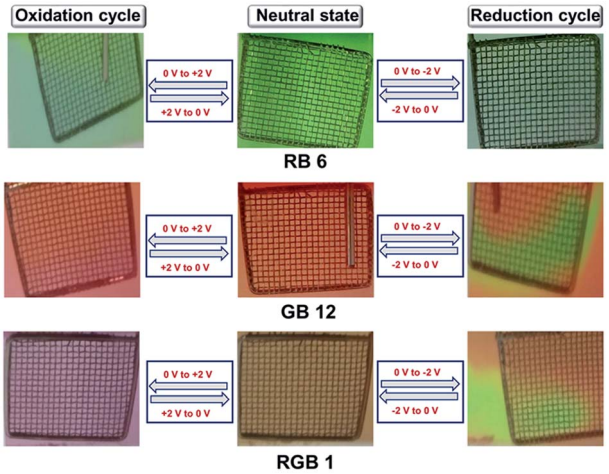

Fig. 5 Images of solution-phase electrochromism behaviour of RB **6**, GB **12** and RGB antenna **1** during (a) oxidation and (b) reduction processes during spectroelectrochemistry.

pink upon oxidation and bright fluorescent neon-greenish upon reduction and reverted back to the original colour of the neutral state upon reversion of the voltage applied (Fig. 5). RGB **1** was brown in the neutral state that reversibly turned to dark purple upon oxidation and to fluorescent neon-green in the reduction cycle (Fig. 5). Thus, all these compounds serve as reversible electrochromic switches in the solution phase and have potential applications as switchable redox sensors.

Furthermore, electrochemical experiments were performed on thin films of GB **12** and RGB antenna **1** spin coated onto indium tin oxide (ITO) plates using $CHCl_3$ solutions (10^{-2} M) and a three electrode set-up with ITO as the working electrode, a Pt wire as the counter electrode and Ag/AgCl as the reference electrode and after experiment their absorption and transmittance spectra were recorded.[47,62–65] Acetonitrile being an orthogonal solvent was used for performing the CV with addition of tetrabutylammonium hexafluorophosphate (TBAHFP) supporting electrolyte. GB antenna **12** was red in the neutral state and with application of positive potential from 0 to +2 V, the red colour disappeared and changed to colourless while with negative potential from 0 to −2 V, first the red colour changed to green and finally it became colourless (Fig. S10a‡). Similarly, RGB antenna **1** was brown in the neutral state, and with application of positive potential from 0 to +2 V, it changed to colourless and upon applying negative potential from 0 to −2 V, the brown colour changed first to a dark green colour which finally changed to transparent (Fig. S10b‡). The corresponding absorption (Fig. S11‡) and transmittance spectra (Fig. S12‡) for neutral thin films and for oxidized and reduced thin films for GB **12** and RGB **1** are provided in the ESI.‡ This experiment could not be performed with RB **6** because of its solubility in acetonitrile.

Acid/base sensing

The responsiveness of optical properties of RGB antenna **1**, RB **6** and GB **12** to acids was investigated by addition of

Open Access Article. Published on 15 November 2021. Downloaded on 2/20/2026 10:56:39 PM. This article is licensed under a Creative Commons Attribution-NonCommercial 3.0 Unported Licence.

trifluoroacetic acid (TFA) and monitoring their absorption and emission profiles (Fig. 6 and S13–S22‡). Upon increasing the TFA amount from 0 to 74 667 equivalents (equiv.) in a $CHCl_3$ solution of **1**, the absorption band of Np at 436 nm showed a drastic decrease[53] and a red shift to 447 nm (Fig. 6a). The absorbance of the PDI band showed a negligible red shift of ~10 nm and absorbance of aza-BODIPY showed a slight blue shift of ~8 nm and the RGB antenna was thus converted into a predominantly RG antenna (Fig. 6a) and corresponding emission spectra are shown in Fig. 6b. Upon back titrating the solution of antenna **1** with triethylamine (TEA), the blue absorption was recovered completely and thus the RG antenna was reversibly converted to RGB antenna **1** (Fig. S19a‡). The titration of RB **6** with increasing amounts of acid led to depletion of the absorption band at 436 nm (Fig. 6c). For RB antenna **6** with addition of acid, the fluorescence intensities of both PDI and aza-BODIPY decreased upon excitation at 396 nm. The corresponding emission spectra are shown in Fig. 6d. Interestingly, upon excitation at 396 nm, the emission colours showed a transition from green to blue through a single component white light emission with CIE coordinates of (0.32, 0.33) (Fig. 6e) at a particular equiv. of TFA (~22 003 equiv.). The same solution however when excited at 442 nm, showed emission colours transitioning from green (0.34, 0.56) to yellow (0.40, 0.44) (Fig. 6f). Thus, reversible optical switching through acids and bases could be achieved for RGB **1** (*i.e.*, RGB ↔ RG).

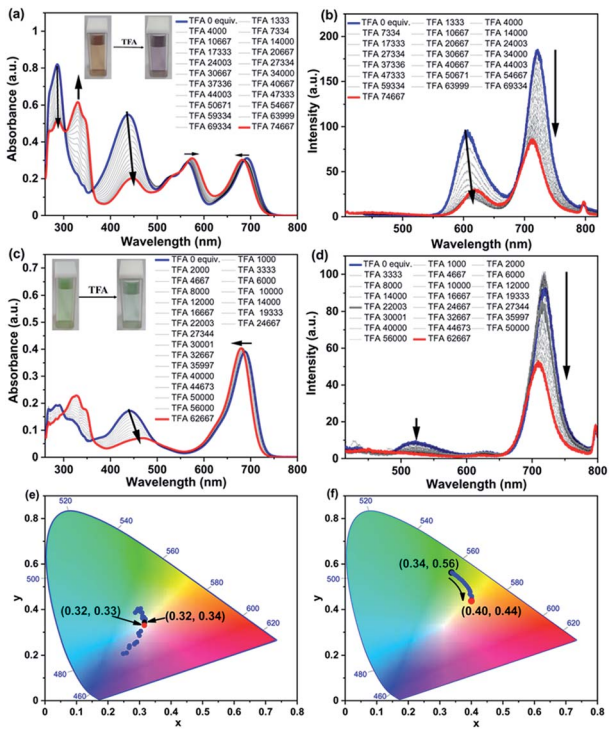

Fig. 6 Absorption and emission (λ_{ex} = 396 nm) spectra on titration with TFA (a) and (b) of RGB **1**; (c) and (d) of RB **6**; chromaticity plot (e) (λ_{ex} = 396 nm) and (f) (λ_{ex} = 442 nm) for **6** in $CHCl_3$ (c ~ 5 μM). Initial and final spectra are represented by blue and red colours respectively.

On the addition of acid, the depletion in the Np absorption band can be attributed to the protonation of the amine nitrogen atom which led to conjugation break and hence the loss of colour. For the PDI band, with addition of acid the red shift and loss of intensity are reported in the literature[66] where firstly, TFA molecules form H-bonding with imide –C═O units and then with bay position connected –O– atoms of PDI which led to a decrease in the energy gap between the HOMO and LUMO and resulted in a red shift. The loss of fluorescence intensity could be attributed to the electron transfer process between bay position H-bonded TFA molecules and the central PDI moiety.[66] For aza-BODIPY, with the addition of TFA, a blue shift occurs presumably due to the H-bonding between TFA molecules and –O– atoms (Fig. 7).

In addition to acid/base sensitivity of these compounds in organic solvents, their pH sensing capabilities were also checked in aqueous solvents, similar to literature known example.[67] Thus, pH titration experiments were performed in semi-aqueous solvent combinations (tetrahydrofuran (THF)/water 25/75 v/v) for antennae RB **6**, GB **12** and RGB **1** where aqueous buffer was used. The UV/Vis titration at different pH and plots of absorbance *vs.* pH are shown in Fig. S23 in ESI.‡ Upon decrease in pH, these antennae showed most pronounced depletion of the Np absorption band in the pH range of 7–4 and there by showed reasonable pH sensitivity in the range of pH 4–7.

Metal sensing

To explore the optical response of RGB antenna **1** towards metal ions, spectroscopic studies were performed with addition of metal ions. We recently reported that the aza-BODIPY moiety in FRET cassettes undergo a redox transformation in the presence of Fe^{3+} and Co^{2+} that leads to the depletion of its absorption band due to radical cation/anion generation leading to a ratiometric FRET turn-off sensing behavior.[68]

Different metal ions such as Ag^{+}, Na^{+}, K^{+}, Li^{+}, Mg^{2+}, Ba^{2+}, Mn^{2+}, Ni^{2+}, Pb^{2+}, Co^{2+}, Cu^{2+}, Fe^{2+}, Zn^{2+}, Cd^{2+}, and Al^{3+} were added to a solution of RGB antenna **1** in THF and the absorption and emission spectra were recorded (Fig. S26 and S27‡). Among all metals, antenna **1** was responsive to only Fe^{3+} and Co^{2+} characterized by a significant depletion of the aza-BODIPY band. As a result of depleted aza-BODIPY absorption in the presence of Co^{2+} and Fe^{3+}, its spectral overlap with PDI reduced drastically leading to FRET turn-off. UV/Vis and fluorescence

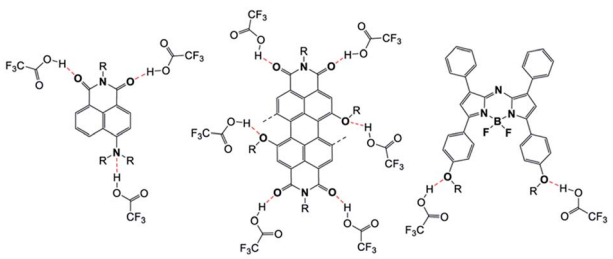

Fig. 7 Basic representation of protonation/H-bonding sites between TFA molecules and respective Np, PDI and aza-BODIPY moieties.

© 2021 The Author(s). Published by the Royal Society of Chemistry

Open Access Article. Published on 15 November 2021. Downloaded on 2/20/2026 10:56:39 PM.
This article is licensed under a Creative Commons Attribution-NonCommercial 3.0 Unported Licence.

titrations of **1** with Co^{2+} (Fig. 8a, b) and Fe^{3+} (Fig. 8c, d) were performed and the emission data in the two channels were used to calculate the association constants using the Merkx model[69] for ratiometric fluorescence in the two emission channels. Accordingly, association constants of 10.25×10^4 M^{-1} and 2.94×10^4 M^{-1} (Table S8‡) were obtained for RGB antenna **1** for its binding to Co^{2+} and Fe^{3+} respectively (Fig. S28 and S29‡). Thus, metal ion induced modulation of the R band led to conversion of the RGB antenna into a GB antenna (RGB → GB). The corresponding Jobs plots of RGB antenna **1** with Co^{2+} and Fe^{3+} led to a possible binding stoichiometry of 1 : 2 for both **1**: Co^{2+} and **1**: Fe^{3+} (Fig. S30‡). In a similar manner, UV/Vis and fluorescence titrations of RB antenna **6** were performed with Co^{2+} (Fig. S31‡) and Fe^{3+} (Fig. S33‡). From the emission titration, association constants of 12.90×10^4 M^{-1} and 4.17×10^4 M^{-1} (Table S7‡) were obtained respectively for Co^{2+} (Fig. S32‡) and Fe^{3+} respectively using the Merkx model (Fig. S34‡). The origin of high selectivity of Fe^{3+} can be explained based on the calculated charge density value ($\rho \sim 4.30$) which is the highest among those of first row transition metals and alkaline earth metals.[70] Due to the highest charge density of Fe^{3+}, it can form complexes with electron deficient aza-BODIPY. Furthermore, Fe^{3+} by virtue of its two accessible oxidation states (*i.e.*, +2 and +3), can participate in electron transfer processes[71] which are otherwise not possible if the metal has only one accessible oxidation state. Previously we have elucidated that the sensing of Co^{2+} and Fe^{3+} sensing by aza-BODIPY is a redox-driven process.[68] The same rationale can be applied to Co^{2+}, since it can readily adopt +2 or +3 states and can therefore participate in charge transfer processes to or from aza-BODIPY. The plausible mechanism for Co^{2+}/Fe^{3+} ions sensing is provided in the ESI.‡ A comparison table for all the literature reported RGB systems (polymers, self-assembled materials, covalently connected chromophores, peptide scaffolds *etc.*) with their applications in sensing and in other areas is presented in ESI, Table S8.‡

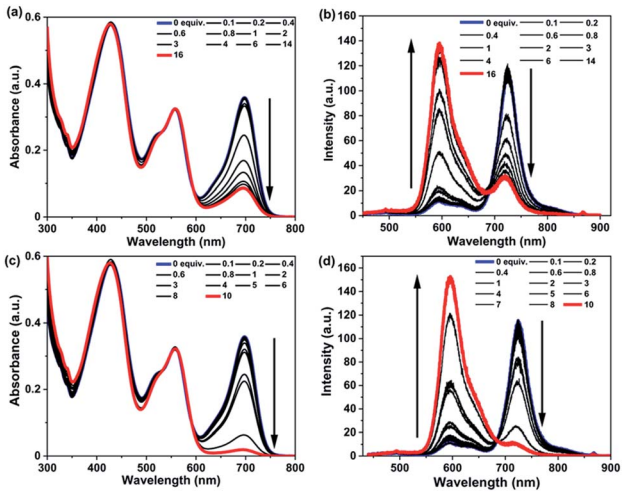

Fig. 8 Absorption and emission spectra of RGB antenna **1** ($\lambda_{ex} = 430$ nm) ($c \sim 5$ μM) on titration with increasing equivalents of (a) and (b) Co^{2+}; (c) and (d) Fe^{3+} perchlorate salts in THF. Initial and final spectra are represented by blue and red colours respectively.

Switchable or tunable fluorescent inks

The tunability of spectral properties of model antennae RB **6**, GB **12** and final RGB antenna **1** with different stimuli inspired us to utilize these antennae as switchable fluorescent inks.[72–79] Firstly, antenna-poly(methyl methacrylate (PMMA) composites were prepared by dissolving RB **6**, GB **12** and RGB **1** ($c \sim 10^{-3}$ M) and PMMA (1 wt%) in chloroform. Filter paper with text written with RB **6**-PMMA composite appeared yellowish green under normal light which on exposure to TFA changed to an olive green colour and comes back to the original colour after ~5 minutes (Fig. 9a). GB **12**-PMMA composite coated on filter paper showed bright orange fluorescence which on exposure to TFA changed to pink and after ~5 minutes returned to the original colour, while with heat (~60 °C) it changed to a dull orange colour and the original colour was recovered upon cooling down

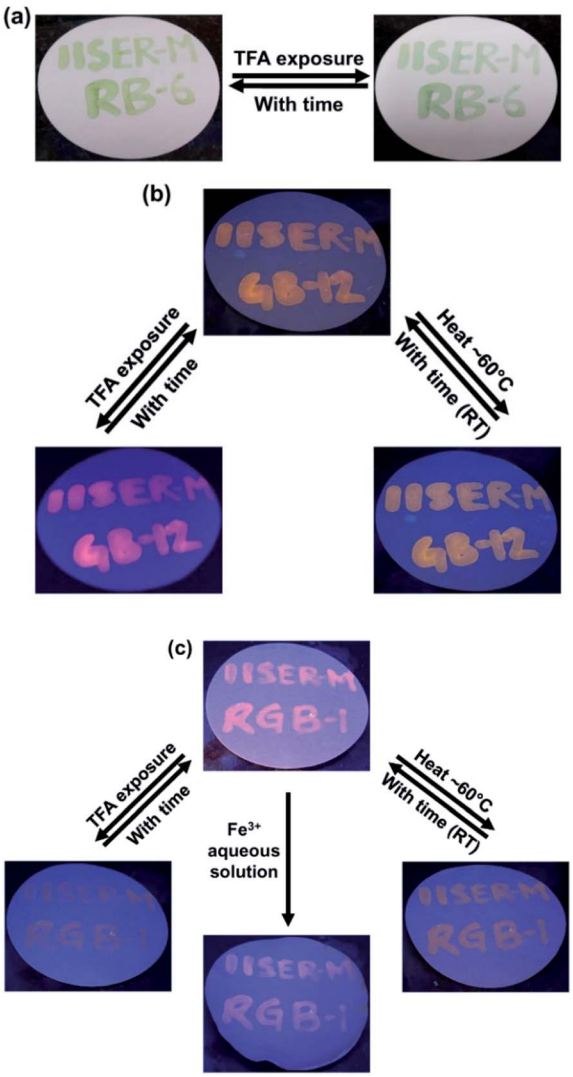

Fig. 9 (a) Reversible colour change of text written with the RB **6**-PMMA (1 wt%) solution in $CHCl_3$ on filter paper upon TFA exposure (picture taken in day light); similar fluorescent inks based on text written on filter paper with (b) GB **12**-PMMA and (c) RGB **1**-PMMA solutions in $CHCl_3$ under different stimuli such as TFA vapour, temperature and Fe^{3+} aqueous solution. (UV light; $\lambda_{ex} = 365$ nm).

Open Access Article. Published on 15 November 2021. Downloaded on 2/20/2026 10:56:39 PM. This article is licensed under a Creative Commons Attribution-NonCommercial 3.0 Unported Licence.

to room temperature (RT) (Fig. 9b). RGB antenna **1**-PMMA composite was used to write text on a filter paper that showed reddish emission which on TFA exposure became very faint and almost invisible to the naked eye and was recovered to the initial colour with time. On heating (~60 °C) RGB **1**-PMMA the initial reddish fluorescence changed to orange and after cooling down to RT it reverted back to the original colour. On dipping the filter paper with text written using RGB **1**-PMMA in aqueous Fe^{3+} solution, followed by washing and drying, the fluorescence changed irreversibly from reddish to very pale orange (Fig. 9c). Such fluorescent inks that are responsive to multiple stimuli as demonstrated can potentially serve in anti-counterfeiting applications and technologies.

Conclusions

In summary, a RGB multichromophoric antenna **1** with Np and PDI as energy donors and a central aza-BODIPY energy acceptor was designed that showed efficient cascade FRET of ~100% from peripheral Nps and PDIs to central aza-BODIPY. RGB antenna **1** showed pronounced temperature-dependent emission behaviour where intensities in two emission channels could be tuned in opposite directions by temperature variation giving rise to a unique ratiometric sensing with a sensitivity of 0.4% °C. RB **6**, GB **12** and RGB **1** showed distinct solution phase electrochromism. Upon variation in pH, RGB antenna **1** showed a reversible absorption modulation in the blue absorption region (RGB ↔ RG). Furthermore, RGB antenna **1** was utilized to selectively sense Co^{2+} and Fe^{3+} through a FRET turn-off mechanism induced by a redox process at the aza-BODIPY site that manifested as a spectral modulation in the red region (RGB → GB). White light emission with CIE coordinates (0.32, 0.33) was obtained for RB **6** at a particular equiv. of TFA (~22 003 equiv.). Such a multifunctional FRET based RGB antenna is a powerful sensor for precise multiparameter (temperature, pH, metal ions) detection and sensing. Applications of such multifunctional small molecular sensors in detection of pH, temperature or metal ions in cellular microenvironments are thus envisaged and will be pursued in future. Furthermore, these antennae-PMMA polymer composites were utilized as reversible thermo-responsive, acid sensitive and metal ion sensitive irreversible fluorescent inks.

Data availability

Experimental data associated with this work have been provided in the ESI.‡

Author contributions

The manuscript was written through contributions of all the authors. All authors have given approval to the final version of the manuscript.

Conflicts of interest

There are no conflicts to declare.

Acknowledgements

This work was financially supported by IISER Mohali and DST (DST/TM/SERI/FR/162) and K. R. thanks CSIR for a PhD fellowship. The authors sincerely acknowledge central NMR and mass facilities as well as various departmental facilities of IISER Mohali. The authors like to thank the anonymous reviewers whose suggestions have helped in improving the quality of the manuscript.

Notes and references

1 G. D. Scholes, G. R. Fleming, A. Olaya-Castro and R. van Grondelle, *Nat. Chem.*, 2011, **3**, 763–774.
2 A. Harriman, *Chem. Commun.*, 2015, **51**, 11745–11756.
3 T. Mirkovic, E. E. Ostroumov, J. M. Anna, R. van Grondelle, Govindjee and G. D. Scholes, *Chem. Rev.*, 2017, **117**, 249–293.
4 D. Gust, T. A. Moore and A. L. Moore, *Acc. Chem. Res.*, 2001, **34**, 40–48.
5 T. Brixner, R. Hildner, J. Köhler, C. Lambert and F. Würthner, *Adv. Energy Mater.*, 2017, **7**, 1–33.
6 G. McDermott, S. M. Prince, A. A. Freer, A. M. Hawthornthwaite-Lawless, M. Z. Papiz, R. J. Cogdell and N. W. Isaacs, *Nature*, 1995, **374**, 517–521.
7 W. Kühlbrandt, D. N. Wang and Y. Fujiyoshi, *Nature*, 1994, **367**, 614–621.
8 T. Keijer, T. Bouwens, J. Hessels and J. N. H. Reek, *Chem. Sci.*, 2021, **12**, 50–70.
9 R. Ziessel and A. Harriman, *Chem. Commun.*, 2011, **47**, 611–631.
10 T. T. T. Nguyen, D. Türp, D. Wang, B. Nölscher, F. Laquai and K. Müllen, *J. Am. Chem. Soc.*, 2011, **133**, 11194–11204.
11 K. R. J. Thomas, A. L. Thompson, A. V. Sivakumar, C. J. Bardeen and S. Thayumanavan, *J. Am. Chem. Soc.*, 2005, **127**, 373–383.
12 T. Weil, E. Reuther, C. Beer and K. Müllen, *Chem.–Eur. J.*, 2004, **10**, 1398–1414.
13 N. Aratani, D. Kim and A. Osuka, *Acc. Chem. Res.*, 2009, **42**, 1922–1934.
14 L. Beverina, G. A. Pagani and M. Sassi, *Chem. Commun.*, 2014, **50**, 5413–5430.
15 D. Holten, D. F. Bocian and J. S. Lindsey, *Acc. Chem. Res.*, 2002, **35**, 57–69.
16 Y. Nakamura, N. Aratani and A. Osuka, *Chem. Soc. Rev.*, 2007, **36**, 831–845.
17 S. Sengupta and F. Würthner, *Acc. Chem. Res.*, 2013, **46**, 2498–2512.
18 Q. Zou, K. Liu, M. Abbas and X. Yan, *Adv. Mater.*, 2016, **28**, 1031–1043.
19 K. V. Rao, K. K. R. Datta, M. Eswaramoorthy and S. J. George, *Adv. Mater.*, 2013, **25**, 1713–1718.
20 H. Peng, L. Niu, Y. Chen, L. Wu, C. Tung and Q. Yang, *Chem. Rev.*, 2015, **115**, 7502–7542.
21 J. Fan, M. Hu, P. Zhan and X. Peng, *Chem. Soc. Rev.*, 2013, **42**, 29–43.
22 J.-J. Li, H.-Y. Zhang, X.-Y. Dai, Z.-X. Liu and Y. Liu, *Chem. Commun.*, 2020, **56**, 5949–5952.

© 2021 The Author(s). Published by the Royal Society of Chemistry

Open Access Article. Published on 15 November 2021. Downloaded on 2/20/2026 10:56:39 PM. This article is licensed under a Creative Commons Attribution-NonCommercial 3.0 Unported Licence.

23 J. M. Serin, D. W. Brousmiche and J. M. J. Fréchet, *Chem. Commun.*, 2002, **2**, 2605–2607.
24 T. Weil, E. Reuther and K. Müllen, *Angew. Chem., Int. Ed.*, 2002, **41**, 1900–1904.
25 W. R. Dichtel, S. Hecht and J. M. J. Fréchet, *Org. Lett.*, 2005, **7**, 4451–4454.
26 R. Métivier, F. Kulzer, T. Weil, K. Müllen and T. Basché, *J. Am. Chem. Soc.*, 2004, **126**, 14364–14365.
27 M. Cotlet, T. Vosch, S. Habuchi, T. Weil, K. Müllen, J. Hofkens and F. De Schryver, *J. Am. Chem. Soc.*, 2005, **127**, 9760–9768.
28 O. Altan Bozdemir, S. Erbas-Cakmak, O. O. Ekiz, A. Dana and E. U. Akkaya, *Angew. Chem., Int. Ed.*, 2011, **50**, 10907–10912.
29 R. Ziessel, G. Ulrich, A. Haefele and A. Harriman, *J. Am. Chem. Soc.*, 2013, **135**, 11330–11344.
30 S. Diring, F. Puntoriero, F. Nastasi, S. Campagna and R. Ziessel, *J. Am. Chem. Soc.*, 2009, **131**, 6108–6110.
31 A. Uetomo, M. Kozaki, S. Suzuki, K. Yamanaka, O. Ito and K. Okada, *J. Am. Chem. Soc.*, 2011, **133**, 13276–13279.
32 A. Harriman, L. J. Mallon, S. Goeb, G. Ulrich and R. Ziessel, *Chem.–Eur. J.*, 2009, **15**, 4553–4564.
33 A. Harriman, L. Mallon and R. Ziessel, *Chem.–Eur. J.*, 2008, **14**, 11461–11473.
34 C. Lambert, J. Hoche, M. H. Schreck, M. Holzapfel, A. Schmiedel, J. Selby, A. Turkin and R. Mitric, *J. Phys. Chem. A*, 2021, **125**, 2504–2511.
35 L. Rocard, D. Wragg, S. A. Jobbins, L. Luciani, J. Wouters, S. Leoni and D. Bonifazi, *Chem.–Eur. J.*, 2018, **24**, 16136–16148.
36 P. Ensslen and H. A. Wagenknecht, *Acc. Chem. Res.*, 2015, **48**, 2724–2733.
37 O. Kulyk, L. Rocard, L. Maggini and D. Bonifazi, *Chem. Soc. Rev.*, 2020, **49**, 8400–8424.
38 G. J. Hedley, A. Ruseckas and I. D. W. Samuel, *Chem. Rev.*, 2017, **117**, 796–837.
39 Z. Zhang, Z. Zhao, Y. Hou, H. Wang, X. Li, G. He and M. Zhang, *Angew. Chem., Int. Ed.*, 2019, **58**, 8862–8866.
40 M. Li, S. Long, Y. Kang, L. Guo, J. Wang, J. Fan, J. Du and X. Peng, *J. Am. Chem. Soc.*, 2018, **140**, 15820–15826.
41 M. Li, A. Lee, K. L. Kim, J. Murray, A. Shrinidhi, G. Sung, K. M. Park and K. Kim, *Angew. Chem., Int. Ed.*, 2018, **57**, 2120–2125.
42 L. Wu, C. Huang, B. P. Emery, A. C. Sedgwick, S. D. Bull, X. P. He, H. Tian, J. Yoon, J. L. Sessler and T. D. James, *Chem. Soc. Rev.*, 2020, **49**, 5110–5139.
43 M. M. A. Mazza and F. M. Raymo, *J. Mater. Chem. C*, 2019, **7**, 5333–5342.
44 E. J. McLaurin, L. R. Bradshaw and D. R. Gamelin, *Chem. Mater.*, 2013, **25**, 1283–1292.
45 H. Zhang, Y. Zhai, M. Wang, S. Dong, Y. Fang and L. Zhang, *Nanoscale*, 2019, **11**, 3718–3724.
46 P. Q. Nhien, W. L. Chou, T. T. K. Cuc, T. M. Khang, C. H. Wu, N. Thirumalaivasan, B. T. B. Hue, J. I. Wu, S. P. Wu and H. C. Lin, *ACS Appl. Mater. Interfaces*, 2020, **12**, 10959–10972.
47 Q. Zhang, C. Y. Tsai, L. J. Li and D. J. Liaw, *Nat. Commun.*, 2019, **10**, 2–9.
48 C. Maiti and D. Dhara, *Langmuir*, 2017, **33**, 12130–12139.
49 F. C. Liang, C. C. Kuo, B. Y. Chen, C. J. Cho, C. C. Hung, W. C. Chen and R. Borsali, *ACS Appl. Mater. Interfaces*, 2017, **9**, 16381–16396.
50 C. Li, Y. Zhang, J. Hu, J. Cheng and S. Liu, *Angew. Chem., Int. Ed.*, 2010, **49**, 5120–5124.
51 Z. Xu, S. Peng, Y.-Y. Wang, J.-K. Zhang, A. I. Lazar and D.-S. Guo, *Adv. Mater.*, 2016, **28**, 7666–7671.
52 X. Wan and S. Liu, *J. Mater. Chem.*, 2011, **21**, 10321–10329.
53 H. Q. Dong, T. B. Wei, X. Q. Ma, Q. Y. Yang, Y. F. Zhang, Y. J. Sun, B. B. Shi, H. Yao, Y. M. Zhang and Q. Lin, *J. Mater. Chem. C*, 2020, **8**, 13501–13529.
54 F. Würthner, C. R. Saha-Möller, B. Fimmel, S. Ogi, P. Leowanawat and D. Schmidt, *Chem. Rev.*, 2016, **116**, 962–1052.
55 Y. Ge and D. F. O'Shea, *Chem. Soc. Rev.*, 2016, **45**, 3846–3864.
56 F. Schweighöfer, L. Dworak, C. A. Hammer, H. Gustmann, M. Zastrow, K. Rück-Braun and J. Wachtveitl, *Sci. Rep.*, 2016, **6**, 1–9.
57 V. Sláma, V. Perlík, H. Langhals, A. Walter, T. Mančal, J. Hauer and F. Šanda, *Front. Chem.*, 2020, **8**, 1–12.
58 H. Langhals, S. Poxleitner, O. Krotz, T. Pust and A. Walter, *Eur. J. Org. Chem.*, 2008, 4559–4562.
59 H. Langhals and A. Walter, *J. Phys. Chem. A*, 2020, **124**, 1554–1560.
60 W. Zhang, J. Li, H. Lei and B. Li, *Opt. Express*, 2020, **28**, 12450–12459.
61 Z. Zhang, Z. Zhao, L. Wu, S. Lu, S. Ling, G. Li, L. Xu, L. Ma, Y. Hou, X. Wang, X. Li, G. He, K. Wang, B. Zou and M. Zhang, *J. Am. Chem. Soc.*, 2020, **142**, 2592–2600.
62 P. Monk, R. Mortimer and D. Rosseinsky, in *Electrochromism and Electrochromic Devices*, Cambridge University Press, Cambridge, 2009, pp. 1–24.
63 H. Lim, S. Seo, S. Pascal, Q. Bellier, S. Rigaut, C. Park, H. Shin, O. Maury, C. Andraud and E. Kim, *Sci. Rep.*, 2016, **6**, 1–8.
64 W. Q. Deng, A. H. Flood, J. F. Stoddart and W. A. Goddard, *J. Am. Chem. Soc.*, 2005, **127**, 15994–15995.
65 N. Elool Dov, S. Shankar, D. Cohen, T. Bendikov, K. Rechav, L. J. W. Shimon, M. Lahav and M. E. Van Der Boom, *J. Am. Chem. Soc.*, 2017, **139**, 11471–11481.
66 X. Yu, C. Zhan, X. Ding, S. Zhang, X. Zhang, H. Liu, L. Chen, Y. Wu, H. Fu, S. He, Y. Huang and J. Yao, *Phys. Chem. Chem. Phys.*, 2013, **15**, 11960–11965.
67 Y. Tu, Y. Ju, D. Xiao, J. Liu, Z. Zhao, Z. Liu, J. W. Y. Lam and B. Z. Tang, *Adv. Sci.*, 2020, **7**, 1–9.
68 K. Rani, U. K. Pandey and S. Sengupta, *J. Mater. Chem. C*, 2021, **9**, 4607–4618.
69 A. M. Hessels and M. Merkx, *ACS Sens*, 2016, **1**, 498–502.
70 S. Huang, P. Du, C. Min, Y. Liao, H. Sun and Y. Jiang, *J. Fluoresc.*, 2013, **23**, 621–627.
71 S. D. Padghan, R. S. Bhosale, S. V. Bhosale, F. Antolasic, M. Al Kobaisi and S. V. Bhosale, *Molecules*, 2017, **22**, 1417.
72 E. R. Sauvé, C. M. Tonge and Z. M. Hudson, *J. Am. Chem. Soc.*, 2019, **141**, 16422–16431.
73 X. Chen, J. Chen, G. Sun, L. Guo, J. Su and Z. Zhang, *ACS Appl. Mater. Interfaces*, 2021, **13**, 38629–38636.

© 2021 The Author(s). Published by the Royal Society of Chemistry

Open Access Article. Published on 15 November 2021. Downloaded on 2/20/2026 10:56:39 PM.
This article is licensed under a Creative Commons Attribution-NonCommercial 3.0 Unported Licence.

74 H. J. Kim, D. R. Whang, J. Gierschner, C. H. Lee and S. Y. Park, *Angew. Chem., Int. Ed.*, 2015, **54**, 4330–4333.
75 S. Liu, J. Wang, F. Tang, N. Wang, L. Li, C. Yao and L. Li, *ACS Appl. Mater. Interfaces*, 2020, **12**, 55269–55277.
76 P. Q. Nhien, T. T. K. Cuc, T. M. Khang, C. H. Wu, B. T. B. Hue, J. I. Wu, B. W. Mansel, H. L. Chen and H. C. Lin, *ACS Appl. Mater. Interfaces*, 2020, **12**, 47921–47938.
77 X. C. Yang, Q. Li, M. Tang, Y. L. Yang, W. Yang, J. F. Hu, X. L. Pu, J. Liu, J. T. Zhao and Z. J. Zhang, *ACS Appl. Mater. Interfaces*, 2020, **12**, 20849–20858.
78 J.-C. Yang, Y.-C. Ho and Y.-H. Chan, *ACS Appl. Mater. Interfaces*, 2019, **11**, 29341–29349.
79 P. Gayathri, M. Pannipara, A. G. Al-Sehemi, D. Moon and S. P. Anthony, *Mater. Adv.*, 2021, **2**, 996–1005.

© 2021 The Author(s). Published by the Royal Society of Chemistry